

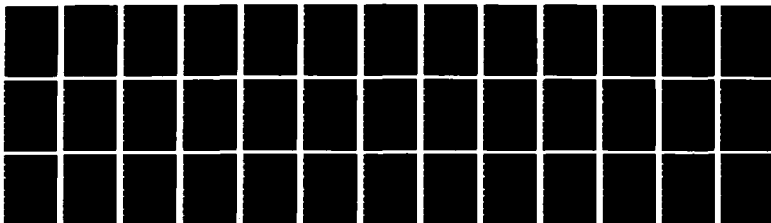
NO-A186 020

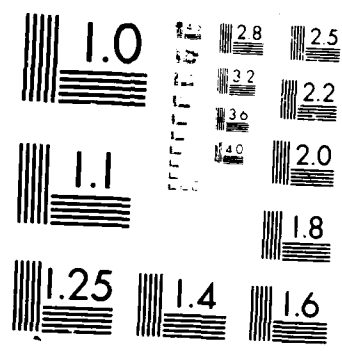
THE RELATIONSHIP OF TENSILE SPECIMEN SIZE AND GEOMETRY
EFFECTS TO UNIQUE (U) NAVAL RESEARCH LAB WASHINGTON DC
P MATIC ET AL 05 OCT 87 NRL-MR-5936

1/1

UNCLASSIFIED

F/G 11/6 1 NL





REPRODUCTION RESOLUTION TEST CHART

Naval Research Laboratory

Washington, DC 20375-5000

DTIC FILE COPY

2



NRL Memorandum Report 5936

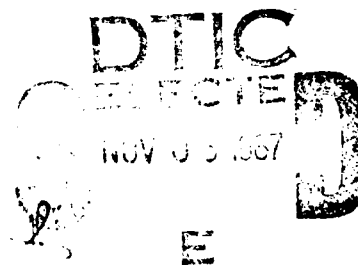
AD-A186 020

**The Relationship of Tensile Specimen
Size and Geometry Effects to
Unique Constitutive Parameters
for Ductile Materials**

PETER MATIC, GEORGE C. KIRBY III AND MITCHELL I. JOLLES

*Mechanics of Materials Branch
Material Science and Technology Division*

October 5, 1987



Approved for public release; distribution unlimited.

308

REPORT DOCUMENTATION PAGE				Form Approved OMB No. 0704-0188	
1a REPORT SECURITY CLASSIFICATION UNCLASSIFIED			1b RESTRICTIVE MARKINGS		
2a SECURITY CLASSIFICATION AUTHORITY			3 DISTRIBUTION/AVAILABILITY OF REPORT		
2b DECLASSIFICATION/DOWNGRADING SCHEDULE			Approved for public release; distribution unlimited.		
4 PERFORMING ORGANIZATION REPORT NUMBER(S) NRL Memorandum Report 5936			5 MONITORING ORGANIZATION REPORT NUMBER(S)		
6a NAME OF PERFORMING ORGANIZATION Naval Research Laboratory		6b OFFICE SYMBOL (If applicable) Code 6382	7a NAME OF MONITORING ORGANIZATION		
6c ADDRESS (City, State, and ZIP Code) Washington, DC 20375-5000			7b ADDRESS (City, State, and ZIP Code)		
8a NAME OF FUNDING/SPONSORING ORGANIZATION Office of Naval Research		8b OFFICE SYMBOL (If applicable)	9 PROCUREMENT INSTRUMENT IDENTIFICATION NUMBER		
8c ADDRESS (City, State, and ZIP Code) Arlington, VA 22217			10 SOURCE OF FUNDING NUMBERS		
PROGRAM ELEMENT NO 61153N22		PROJECT NO RR022- 01-48	TASK NO	WORK UNIT ACCESSION NO DN480-509	
11 TITLE (Include Security Classification) The Relationship of Tensile Specimen Size and Geometry Effects to Unique Constitutive Parameters for Ductile Materials					
12 PERSONAL AUTHOR(S) Matic, Peter, Kirby, G. C. III, and Jolles, Mitchell I.					
13a TYPE OF REPORT		13b TIME COVERED FROM _____ TO _____		14 DATE OF REPORT (Year, Month, Day) 1987 October 5	
15 PAGE COUNT 41					
16 SUPPLEMENTARY NOTATION					
17 COSATI CODES			18 SUBJECT TERMS (Continue on reverse if necessary and identify by block number)		
FIELD	GROUP	SUB-GROUP	Constitutive Tensile necking		
			True stress-true strain Fracture toughness		
			Tensile specimen Energy density		
19 ABSTRACT (Continue on reverse if necessary and identify by block number)					
<p>Straightforward reduction of tensile specimen load-displacement data to uniaxial true stress-true strain data valid at large deformations is not possible for ductile material specimens which exhibit necking. For applications such as fracture mechanics and metal forming processes, valid uniaxial true stress-true strain data is essential for the accurate analysis and prediction of deformations beyond those encountered at incipient necking.</p> <p>This investigation reports on the use of tensile specimen size and geometry effects to accurately and uniquely assess the uniaxial true stress-true strain curve. This is done for a ductile steel in the context of an incremental elastic plastic constitutive theory employing isotropic hardening and a von Mises yield function. Experimental load-displacement data, experimental full field deformation data and the corresponding finite element computational geometries and applied loads for tensile specimen length/diameter ratios are known quantities. The uniaxial true stress-true strain curve parameters and treated as unknown quantities. Successive iteration on the solution curve resulted in successful correlation between the experimental data and computational predictions for all four specimens considered.</p>					
(Continues)					
20 DISTRIBUTION/AVAILABILITY OF ABSTRACT <input type="checkbox"/> UNCLASSIFIED/UNLIMITED <input checked="" type="checkbox"/> SAME AS RPT <input type="checkbox"/> DTIC USERS			21 ABSTRACT SECURITY CLASSIFICATION UNCLASSIFIED		
22a NAME OF RESPONSIBLE INDIVIDUAL Peter Matic			22b TELEPHONE (Include Area Code) (202) 767-5215		22c OFFICE SYMBOL Code 6382

19. ABSTRACT (Continued)

These results support the view that the onset and evolution of tensile specimen necking may be accurately predicted by computational modeling of the specimen geometry, consequence of the interaction between these three feature when each is correctly assessed. This interaction was responsible for the computational prediction of deformation symmetry breaking in the form of asymmetric necking for high length/diameter ratio specimens. This asymmetry was confirmed by the experimental data. As a result, a priori assumptions of deformation symmetry on the basis of geometric symmetry alone appear to be incorrect for some geometries.

CONTENTS

INTRODUCTION	1
EXPERIMENTAL INVESTIGATION	5
COMPUTATIONAL SIMULATIONS	9
CONTINUUM MATERIAL TOUGHNESS CONCEPTS	22
SUMMARY	26
REFERENCES	26
APPENDIX I — ABAQUS Finite Element Program Formulation	29
APPENDIX II — Laboratory Specimen Imperfections	35

Approved For	
1.11.11.11.11	<input checked="" type="checkbox"/>
1.11.11.11.11	<input type="checkbox"/>
1.11.11.11.11	<input type="checkbox"/>
By	
Date	
Approved For	
Date	

A-1



THE RELATIONSHIP OF TENSILE SPECIMEN SIZE AND GEOMETRY EFFECTS TO UNIQUE CONSTITUTIVE PARAMETERS FOR DUCTILE MATERIALS

INTRODUCTION

Accurate knowledge of large deformation ductile material behavior is required for many design and analysis applications. Fracture mechanics and metal forming processes, for example, fall into this category. Two equally important issues make the continuum characterization of inelastic materials in general nontrivial. These issues are (i) the rational development of stress, strain and constitutive formulations for a wide class of materials and (ii) the determination of material constitutive parameters from material test specimen response for use in a particular constitutive formulation. This investigation will deal primarily with the second issue as it applies to a conventional incremental elastic-plastic material formulation for large deformation and rotations. Accomplishing this requires quantitative determination of a material's uniaxial continuum stress versus strain response, valid over its full range of deformation from zero to final fracture.

In the case of ductile metals, the uniaxial tensile test specimen is used to obtain global load-displacement data. In principle, this data can be easily normalized to uniaxial material stress-strain data. From a practical point of view, the necking phenomenon in ductile material specimens has been a formidable barrier to accurate and complete constitutive characterization. As a result, constitutive parameters are usually determined from data obtained prior to necking over the deformation range where purely uniaxial and homogeneous deformations are assumed to exist. The resulting material description is strictly valid only in applications for which the effective stress and strain measures do not exceed the bounds of the uniaxial data. For ductile engineering alloys presently in use, the specimen uniaxial data obtained prior to necking only describes a small portion of the full strain range

experienced by the material from zero deformation to fracture initiation at the center of the neck. This is easily estimated by comparing the uniaxial true strain at the onset of necking with the axial component of strain at the neck (obtained from the initial to final cross section area ratio) when fracture occurs.

Traditional lines of investigation have attributed the onset and subsequent development of necking to either (i) the global instability of deformation predicted by one dimensional formulations, (ii) the presence of specimen geometry imperfections, usually in the form of a specimen taper at the desired neck location, or (iii) material instability criteria which serve to localize deformation. These approaches to explain necking phenomenology are summarized in a review article by Hutchinson (1979). Recent applications of these approaches reported in the literature include Hutchinson et. al. (1983) on neck propagation in polymers and metals, Tvergaard et. al. (1984) on cup-cone tensile fracture, Kleiber (1986) on plastic localization in plain strain and axisymmetric tension and Needleman et al. (1986) on necking and failure in porous plastic solids. Material constitutive parameters are, however, typically obtained from specimen data prior to necking for use in the analysis of necking phenomenon. In a practical sense, this defeats the purpose of the tensile specimen as a means by which to obtain constitutive parameters valid over the full range of material deformation.

Norris et al (1978) developed a uniaxial true stress-true strain relationship through computational simulation of a tensile specimen gage length. Successive iterations on the true stress-true strain relationship were successful in correlating predicted specimen response with laboratory specimen data. The computational model invoked a linear specimen taper, however, to initiate necking at the center of the specimen.

A recent investigation (Matic, 1985) suggests that the onset and evolution of ductile tensile specimen necking is a natural consequence of the interaction between specimen geometry, the physical method of load application and material nonlinearity. No local instability, global instability or geometric imperfections were used to initiate necking. The uniaxial true stress-true strain constitutive

parameters for the behavior of the material at the continuum scale are treated as the unknowns in the problem. The solution curve was constructed to satisfy the requirement that computational simulations of the tensile specimen compare favorably with the measured behavior of the specimen in the laboratory. Examination of the simulation results indicated second order nonuniformity in the stress, strain and energy fields which develop within the specimen gage length immediately upon application of the load. These nonuniformities persist and intensify during subsequent elastic and inelastic deformation of the material. Neck development results after sufficient specimen elongation. Lateral contraction and localization of deformation continue to intensify in the vicinity of the neck. Outside of the neck region, however, the material unloads as the global reaction force decreases in response to the diminishing cross sectional area at the neck.

The presence of deformation inhomogeneity at the onset of specimen yielding is consistent with earlier results. Analytical results of Filon (1902) showed that boundary conditions, representative of physical load application, produce appreciable stress and strain inhomogeneities in elastic circular cylinders subjected to tension or compression loading. Needleman (1972) reported inhomogeneous plastic deformation in circular cylinders at the onset of yielding. The boundary conditions in that study included radial constraint at the ends of the cylinder.

A subsequent computational investigation (Matic and Jolles, 1986) was performed to examine the sensitivity of tensile specimen response to the size and location of a small spherical void defect on the axis of the specimen. The defect was an order of magnitude smaller than the smallest relevant length scale of the specimen, which in this case was the specimen diameter. The results of this investigation suggest that defects of this type and size can be readily responsible for asymmetric deformation and reduced apparent ductility of the specimen.

The results of these two studies suggested that a hybrid computational-experimental technique is a useful methodology, of sufficient sensitivity to the physical parameters of the problem, with which

to determine ductile material constitutive parameters. The combined interaction between specimen geometry, applied load and material behavior, which in combination produce specimen necking, can be used to effectively solve for the material constitutive behavior.

This investigation expanded upon these earlier results to exploit specimen size and geometry effects in conjunction with the computational-experimental approach to determine ductile material constitutive parameters. In this way, the relative sensitivity of the different tensile specimen global responses to the local material response could be evaluated and the ability of a single, unique uniaxial true stress-true strain curve to predict the deformation of different specimens demonstrated. Uniqueness will be referred to in the sense that one uniaxial continuum true stress-true strain curve can predict the behavior of laboratory specimens with different geometries. Twelve different tensile specimen geometries of HY-100 steel were tested in the laboratory. The twelve geometries were generated from four different gage lengths and three different diameters. From these specimens, the four with extreme lengths and diameters were computationally simulated to develop a unique solution curve for the uniaxial true stress-true strain behavior which would adequately predict the corresponding observed specimen behaviors.

In summary, the following approach was used:

- (1) Test a family of uniaxial tensile specimens, featuring four different lengths and three different diameters, to failure.
- (2) Treat the uniaxial continuum true stress-true strain curve as the unknown quantity for computational simulations of the extreme specimen geometries.
- (3) Generate a trial true stress-true strain curve for the computational simulations.
- (4) Compare the predicted axial load-displacement response and full field lateral contraction of the tensile specimens with corresponding data from experiment.

(5) Generate revisions for the true stress-true strain curve if differences between the computational simulations and experiments are greater than desired by repeating steps (3) and (4).

(6) Adopt the final iterate of the true stress-true strain solution curve as the continuum behavior of the material.

EXPERIMENTAL INVESTIGATION

A family of tensile specimens was designed to obtain parametric data on the effects of specimen size and geometry for HY-100 steel. A total of twelve different specimen geometries were examined (Fig. 1). Three specimens of each geometry were tested, plus two extra specimens for the extreme geometries. Three different gage section diameters of 0.76, 1.27 and 1.78 cm (0.30, 0.50 and 0.70in) and four different gage lengths of 1.27, 2.54, 3.81 and 5.08 cm (0.50, 1.00, 1.50 and 2.00in) were used to generate the twelve specimen geometries. These geometries may be described by the gage length to diameter ratio (L_0/D_0). A transition section was included in all specimens between the gage section and the 2.54 cm (1.00in) diameter grip sections over which the load was applied at each end of the specimen. The transition section diameter was sized such that its cross sectional area was double the gage section area. For the material under consideration, this ensured elastic response outside the gage section, geometrically similar transitions for all specimens and more than 1.0" axial distance between grip contact and gage section.

A closed-loop servohydraulic test machine was used to perform the tensile tests. The specimen ends were gripped by hydraulic grips with a grip length of 12.3 cm (3.5in). All tests were performed under stroke control at a rate of 0.127 cm/min (0.050in/min) and a ramp loading function. Prior to testing, the alignment of the grips was checked and was found to be within 0.0051 cm (0.0020in). Thus, no significant bending was introduced.




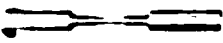





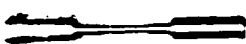
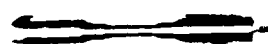

specimen diameter, D_0				specimen length, L_0
0.76 cm	1.27 cm	1.78 cm		
			1.27 cm	
			2.54 cm	
			3.81 cm	
			5.08 cm	

Fig. 1 — Parametric Tensile Specimen Geometries

A clip-on extensometer and a load cell that is an integral part of the load frame were used to measure the elongation of the specimen in the gage length and the applied load. The calibration of the load cell was checked periodically by shunt calibration. The extensometer was calibrated directly by a micrometer and a digital voltmeter. The extensometer calibration was performed whenever a different gage length was used. The voltage readings from the extensometer and the load cell were monitored by two digital voltmeters and converted to digital format. The voltmeters were simultaneously triggered to take data by a microcomputer at 1 second intervals. The microcomputer read the digital voltages from the voltmeters, applied the appropriate calibration factors and wrote the reading number, load and extensometer displacement to a disk. The number of data points per test ranged

between 200 and 300. The microcomputer was also used to start loading of the specimen by triggering a function generator. On screen graphics allowed the test operator to monitor the progress of the test in real time.

A photograph of the specimen's gage length was taken close to the occurrence of the ultimate load. Subsequent photographs were taken in 5 to 10 second intervals until failure. As failure became imminent, the time interval between photographs was decreased. These photographs provided full field specimen deformation information and a means to characterize the neck region after the test was over. Since testing was not halted as the photographs were taken, no load relaxation occurred. However, the corresponding load—displacement data was flagged so that the photograph could be matched with the proper specimen elongation at a later time. Typically, 12 photographs were taken for each specimen.

For each set of specimens of identical geometry, the load (P) versus gage length elongation (δ) responses were essentially identical from the three specimens tested for each of the twelve distinct geometries, demonstrating data reproducibility. The $P - \delta$ data was normalized to engineering stress—engineering strain, i.e.

$$\bar{\sigma} = \frac{P}{A_0} \quad (1)$$

and

$$\bar{\epsilon} = \frac{L - L_0}{L_0} \quad (2)$$

$$= \frac{\delta}{L_0} \quad (3)$$

where A_0 is the undeformed specimen cross section area and L_0 is the undeformed specimen gage length. The data is plotted in Fig. 2 for each gage section diameter with gage section length as a

parameter. The influence of specimen geometry is apparent. The geometric similitude of the neck geometry over all specimens (Fig. 3), with the exception of the specimen with the smallest L_0/D_0 ratio of 0.71 is consistent with the increase in global specimen ductility as the specimen gage section is decreased for a constant specimen diameter.

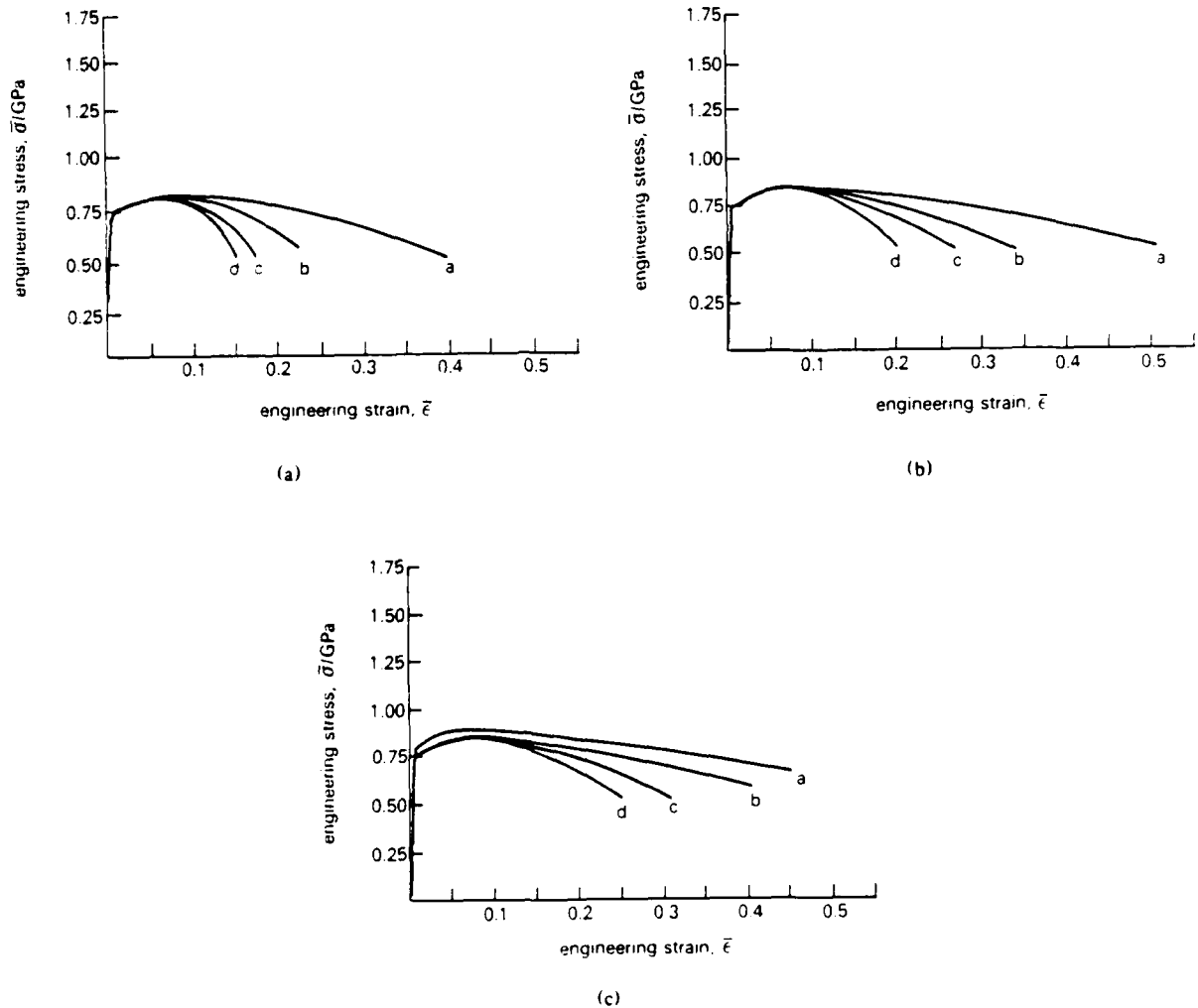


Fig. 2 — Engineering stress-engineering strain curves from experiment. Curves A, B, C and D refer to specimen gage lengths, L_0 , of 1.27, 2.54, 3.81 and 5.08 cm, respectively. Specimen diameter, D_0 , of (a) 0.76 cm, (b) 1.27 cm and (c) 1.78 cm.

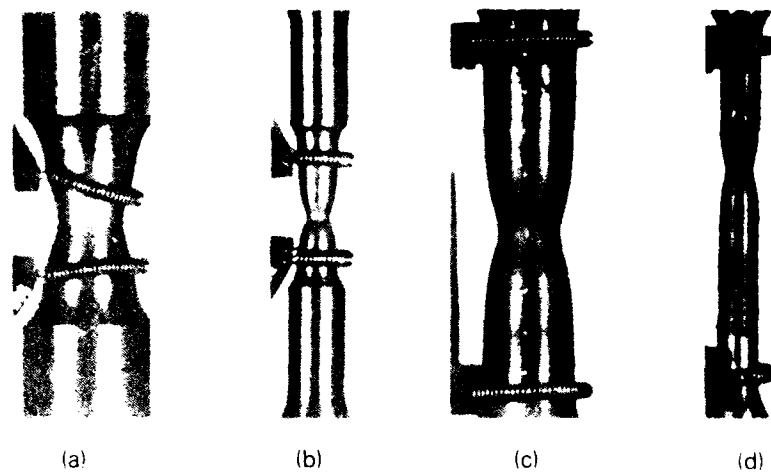


Fig. 3 — Photograph of specimen deformation at the onset of specimen failure for the extreme gage section diameters, D_{01} , and lengths, L_{01} , producing aspect ratios, L_{01}/D_{01} , of (a) 0.71, (b) 1.67, (c) 2.86, and (d) 6.67

COMPUTATIONAL SIMULATIONS

The four extreme specimen geometries, i.e. the specimens featuring 0.76 cm or 1.78 cm (0.30in or 0.70in) diameter and 1.27 cm or 5.08 cm (0.50in or 2.00in) gage length, were selected for computational simulation. If satisfactory predictions of these four specimen responses could be obtained using one unique uniaxial true stress-true strain curve, then the size and geometry independence of the material constitutive characterization would be demonstrated.

The ABAQUS finite element code (Hibbitt et al. 1984b) was used for the computational simulation. The finite element grids for the four specimens are shown in Fig. 4. Axisymmetry of the geometry required that only one-quarter of the specimen be modeled.

Type CAX8H axisymmetric elements were used. These are 8-noded elements with quadratic displacement interpolation and an independently interpolated linear hydrostatic stress. The hydrostatic stress is coupled to the constitutive relation using a Lagrange multiplier. The use of these hybrid elements prevented physically unrealistic displacement constraints from propagating through the grid.

Such constraints can lead to artificially "stiff" responses of standard elements for incompressible or nearly incompressible deformations.

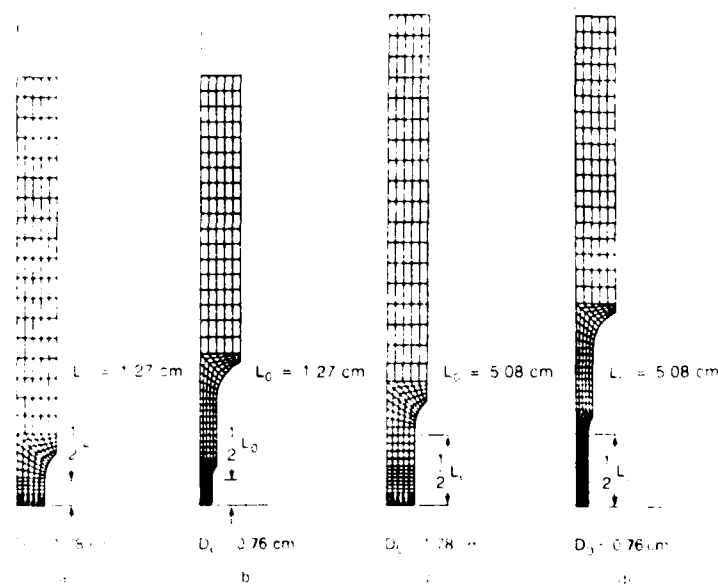


Fig. 4 – Finite element meshes for computational simulations of specimens with aspect ratios, L_0/D_0 , of (a) 0.71, (b) 1.67, (c) 2.86 and (d) 6.67

All analyses were performed with full geometric nonlinearity to account for large strains and large rotations. An updated Lagrangian formulation is used for incremented solutions in ABAQUS. Rik's algorithm, which is load-displacement controlled, was used to ensure numerical stability, since the load decreases for large specimen elongations.

Displacement boundary conditions were prescribed to simulate the physical loading conditions of the laboratory tests. A 6.35 cm (2.50in) wide strip on the lateral surface of the grip section of each specimen was subjected to uniform axial displacements. These conditions reproduced, for computation, the physical nature of the loads applied by the hydraulic grips.

An incremental rate independent plasticity theory was used for the material constitutive model (Hibbitt et al. 1984a). Total strains in the multiaxial strain state ϵ_{ij} are obtained by integration of the

linearly decomposed elastic and plastic components of the rate of deformation tensor D_{ij} . (Refer to Appendix I for a discussion of the ABAQUS finite element program formulation.) This integration is performed under the assumption that the elastic strains remain infinitesimal, as is the case in this investigation. The total multiaxial strain state ϵ_{ij} , expressed in terms of elastic and plastic components, is

$$\epsilon_{ij} = \epsilon_{ij}^e + \epsilon_{ij}^p. \quad (4)$$

The total logarithmic uniaxial strain ϵ , consistent with the integration of the rate of deformation tensor for a multiaxial strain state, is decomposed as

$$\epsilon = \epsilon^e + \epsilon^p \quad (5)$$

The yield function f takes the form

$$f(\tau_{ij}) = \tau(\epsilon^p) \quad (6)$$

where τ_{ij} and τ are multiaxial and uniaxial Kirchhoff (or Trefftz) stress states, respectively. The associated flow rule governs plastic strain increments by the relation

$$d\epsilon_{ij}^p = \lambda \frac{\partial f}{\partial \tau_{ij}} \quad (7)$$

In the case of purely elastic behavior $\lambda = 0$. For active yielding,

$$\lambda > 0 \quad (8)$$

$$\lambda = d\epsilon^p \frac{\tau}{\left[\tau_{ij} \frac{\partial f}{\partial \tau_{ij}} \right]}. \quad (9)$$

Plastic strain increments also satisfy a dissipation equivalence condition

$$\tau d\epsilon^p = \tau_{ij} d\epsilon_{ij}^p \quad (10)$$

and a consistency condition

$$\frac{\partial f}{\partial \tau_{ij}} d\tau_{ij} - \frac{\partial \tau}{\partial \epsilon^p} d\epsilon^p = 0. \quad (11)$$

The von Mises yield function

$$f(\tau_{ij}) = \frac{3}{2} (s_{ij}s_{ij})^{1/2} \quad (12)$$

was employed. The deviatoric stress tensor s_{ij} is defined as

$$s_{ij} = \tau_{ij} - \frac{1}{3} \tau_{kk} \delta_{ij}, \quad (13)$$

where the hydrostatic component of stress is $\tau_{kk}/3$.

The Kirchhoff stress and logarithmic strain measures are employed because of the advantages gained in computational implementation. The Kirchhoff stress tensor τ_{ij} is approximately equal to the more physically motivated Cauchy stress tensor σ_{ij} for deformations involving only small changes in volume. This condition is satisfied in these analyses. The uniaxial true stress-true strain constitutive response of the material is formally input as Cauchy stress and logarithmic strain for the ABAQUS program.

The form of the uniaxial true stress-true strain curve was subject only to the restrictions that it be monotonically increasing and convex. These restrictions are consistent with Drucker's postulates for elastic-plastic constitutive formulations of the type employed here. The curve itself is expressed in a multilinear form as stress and plastic strain pairs supplementing the elastic modulus and Poisson's ratio for the material.

The postulated material true stress-true strain curve was evaluated by one or two of the finite element models per iteration in order to assess its ability to satisfactorily predict the observed responses of these tensile specimens. The following guidelines were developed from the computational simulations conducted in this investigation:

(1) Low L_0/D_0 specimens provide a good gross indication of the material true stress-true strain curve. A larger relative portion of the specimen is part of the necking process, and as a result is under monotonically increasing deformation.

(2) High L_0/D_0 specimens are most useful to guide minor adjustment to the curve obtained from the low L_0/D_0 specimen data. A smaller portion of the higher L_0/D_0 specimens is involved in the actively yielding neck in the specimen. As a result, the balance between the values of stress, strain and tangent modulus of the curve and the relative tendency for the neck to continue deforming while the remainder of the specimen unloads are addressed.

(3) Translation of the material true stress-true strain curve in the stress axis direction results in a comparable translation of the predicted engineering stress-engineering strain curve.

(4) Expansion of the material true stress-true strain curve in the strain axis direction, corresponding to deformation prior to peak engineering stress, tends to accelerate the onset of necking.

(5) Expansion of the material true stress-true strain curve in the strain direction, corresponding to deformation subsequent to peak engineering stress, tends to accelerate the advanced stages of necking.

After approximately five iterations the material true stress-true strain curve, developed using the guidelines listed above, was applied to a full series of analyses performed for all four specimen geometries modeled. The predicted engineering stress-engineering strain curves were in good agreement for the three specimens with the lowest L_0/D_0 ratios of 0.71, 1.67 and 2.33 from the four extreme geometries as used in the development of the material true stress-true strain curve (Fig. 5). The specimen with the highest L_0/D_0 ratio of 6.67 predicted higher engineering strains than anticipated based upon the half-gage length elongations provided by the analyses. In fact, the predicted

engineering stress-engineering strain curve for the high L_0/D_0 specimen was close to that for the second highest L_0/D_0 specimen. This apparent anomaly of one predicted specimen response out of the four, in light of the observed relative sensitivity of the predicted specimen responses to the material true stress-true strain curve, was contrary to what would be anticipated.

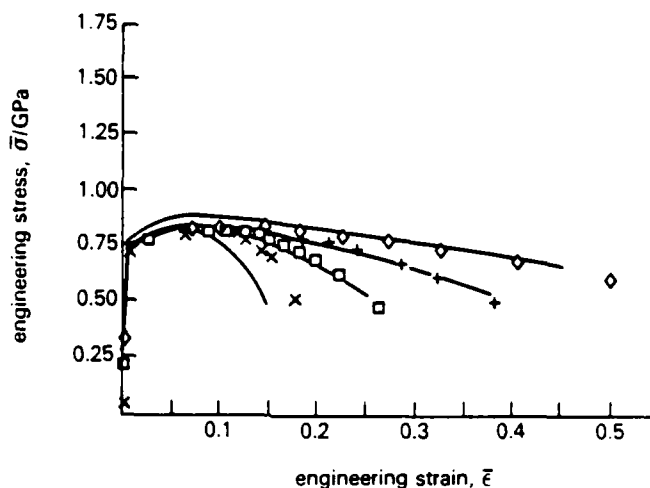


Fig. 5 — Engineering stress-engineering strain curves measured from experiment and predicted by computational simulation allowing for symmetric deformation only: \diamond , $L_0/D_0 = 0.71$; $+$, $L_0/D_0 = 1.67$; \square , $L_0/D_0 = 2.86$; \times , $L_0/D_0 = 6.67$.

Upon examination of deformed shapes (Fig. 6) of the specimens from the analysis, it became apparent that symmetric double necking of the high L_0/D_0 ratio specimen was being predicted, while all three low L_0/D_0 specimen analyses were predicting symmetric single necking. This translated directly into a higher engineering strain for the high L_0/D_0 specimen since one whole neck was present in the half-gage length model, as compared to one-half neck per half-gage length for the three specimens with lower L_0/D_0 ratios. A neck region is, of course, the source of particularly high axial elongations.

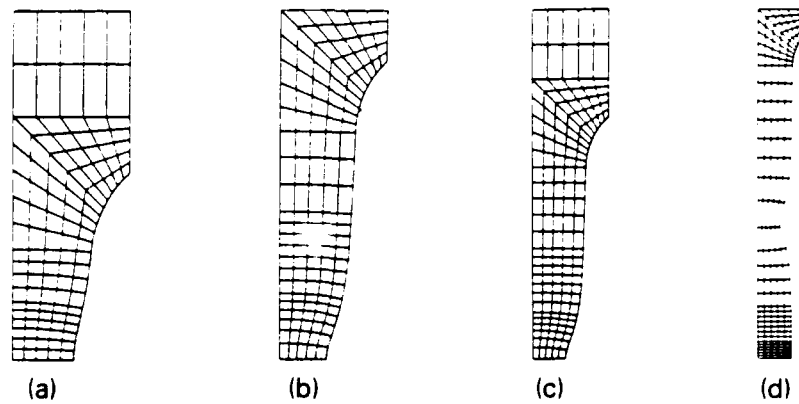


Fig. 6 — Predicted deformation at the onset of specimen failure for aspect ratio, L_0/D_0 , of (a) 0.71, (b) 1.67, (c) 2.86 and (d) 6.67

Symmetric double necking is not physically observed in the laboratory. For it to actually occur, both spatial homogeneity and temporal simultaneity of an extremely high order would have to be present. Without such homogeneity and simultaneity, a single neck would develop asymmetrically, as one necking site would be preferred over another, resulting in monotonically increased loading at the actual necking site and load reduction at the other site, consistent with the results of the other specimens in this study. In order to translate the symmetric double neck results into asymmetric single neck results, the influence of one neck was removed in the following manner.

Surface stretch ratios were approximated using initial nodal coordinates and nodal displacements at the surface (Fig. 7). At the neck locations the strains were significantly higher than those along the remainder of the specimens. To obtain an approximation to the total asymmetric specimen length, the contribution of strains at one neck to the total specimen length were subtracted from the total. The average "background" strain contributions to the specimen length were substituted for the neck segment just removed. The result was a total specimen length based on the contributions of one neck region and a complementary background deformation. Thus,

$$L_{sn} = L_{dn} - L_n + L_h \quad (14)$$

where L_{sn} is the length of the specimen with a single neck, L_{dn} is the length of the specimen with a double neck, L_n is the length contribution of a single neck and L_b is the length contribution due to background deformation outside the neck. The engineering strain for the specimen will be

$$\bar{\epsilon} \approx \frac{L_{sn} - L_0}{L_0} \quad (15)$$

This resulted in good agreement between the engineering stress-engineering strain curve predicted by the analysis and the experimental data for the high L_0/D_0 geometry as seen in Fig. 8.

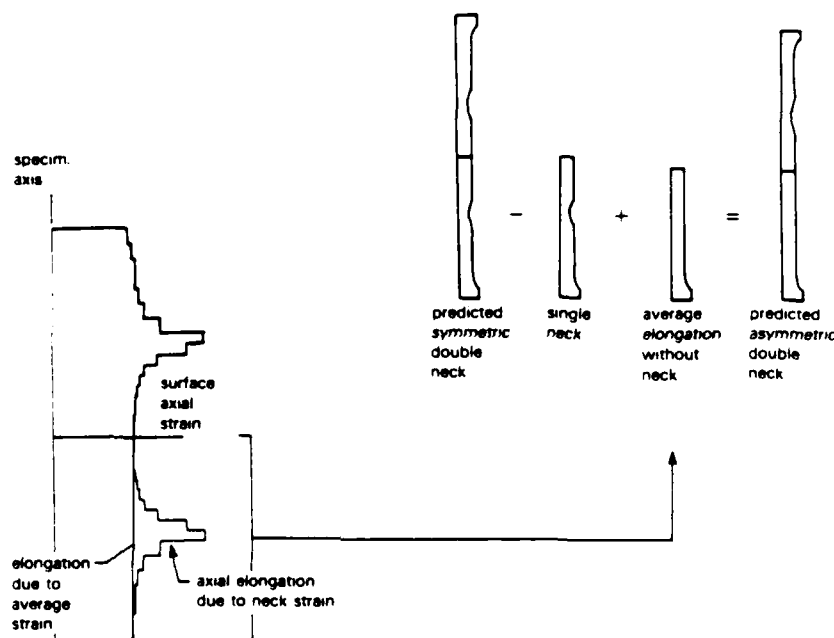


Fig. 7 — Translation of predicted symmetric double neck specimen response into asymmetric single neck specimen response

For this interpretation to be correct, the laboratory tensile specimens should show evidence of symmetric deformation for the three lower L/D specimens and asymmetric deformation for the high L/D specimen. An eccentricity measure to quantitatively describe necking asymmetry may be defined by the expression

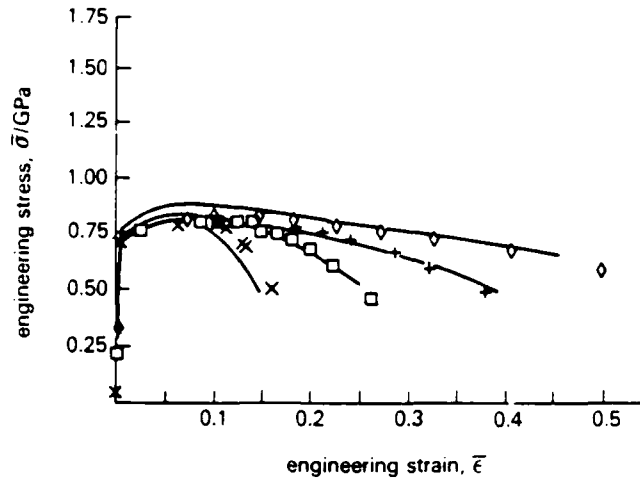


Fig. 8 — Engineering stress-engineering strain curves measured from experiment and predicted by computational simulation allowing for symmetric or asymmetric specimen deformation: \diamond , $L_0/D_0 = 0.71$; +, $L_0/D_0 = 1.67$; \square , $L_0/D_0 = 2.86$; X, $L_0/D_0 = 6.67$.

$$e = \left| 1 - \frac{2z_n}{L} \right| \quad (16)$$

where e is the eccentricity, L is the length of the specimen gage length just prior to specimen fracture and z_n is the distance from a specimen gage mark to the point of minimum specimen diameter. Clearly, when the neck occurs at the center of the specimen, $z_n = L/2$ and therefore $e = 0$. When the neck is at either end of the gage length, $z_n = 0$ or L and therefore $e = 1$. Perfect symmetry coincides with $e = 0$, while maximum possible asymmetry coincides with $e = 1$. These results are plotted in Fig. 9. For L_0/D_0 less than 1.67, the experimental data shows very low values of e , indicating almost perfect symmetry. For L_0/D_0 greater than 1.67, the eccentricity values tend to increase to an average of about 0.5 for L_0/D_0 greater than 4.0.

The computational prediction of asymmetry in specimen deformation is verified by the experimental data. The computational predictions, performed for ideal specimens free of imperfections, establish eccentricity values for comparison purposes. The maximum measured diameter imperfec-

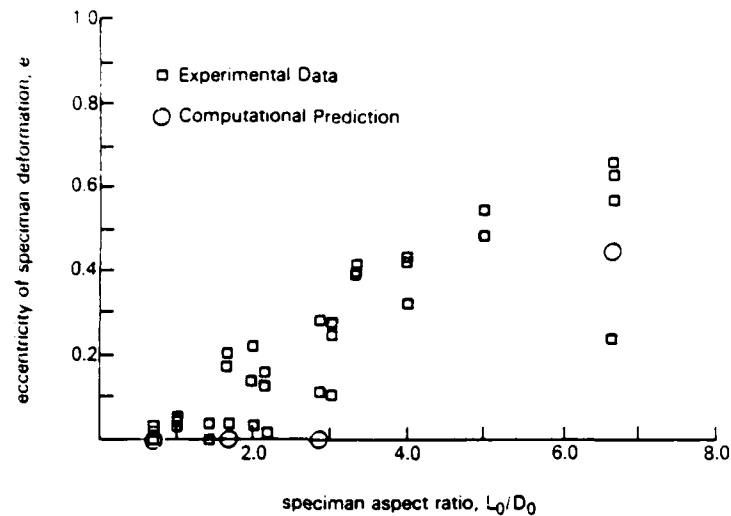


Fig. 9 — Eccentricity, e , of specimen deformation at failure versus specimen aspect ratio, L_0/D_0 : \square , data from experiments; \circ , predictions from computational simulations.

tions exhibited by the laboratory specimens, tabulated in Appendix II, were on the order of 10^{-2} . Imperfections of this magnitude, in line with the conclusions reached by Matic and Jolles (1986) on the role of geometric imperfections in asymmetric necking, are consistent with the measured neck eccentricity values and scatter of the laboratory data as compared to the computationally predicted values.

The hierarchy of imperfections effects is apparent:

- (1) Imperfections are not necessary for necking to occur
- (2) Imperfections which are effectively one order of magnitude smaller than the effective specimen dimension (in this case diameter) are responsible for asymmetric necking
- (3) Symmetry imperfections significantly smaller than the effective imperfection size are sufficient to determine precedence between two apparently simultaneous events at the continuum scale.

The solution curve is shown in Fig. 10. The tabular form for the curve is given in Table 1. The uniaxial continuum true stress-true strain curve show a uniaxial yield stress of $7.17 \times 10^8 \text{ N/m}^2$ (104,000 lb/in²) and a uniaxial maximum stress of just under $1.03 \times 10^9 \text{ N/m}^2$ (150,000 lb/in²). The negligible slope at the higher strain value is consistent with the ductility of HY-100. The notion of a limit load in a rigid—perfectly plastic sense can be viewed as extrapolation back to the stress axis from the maximum stress value.

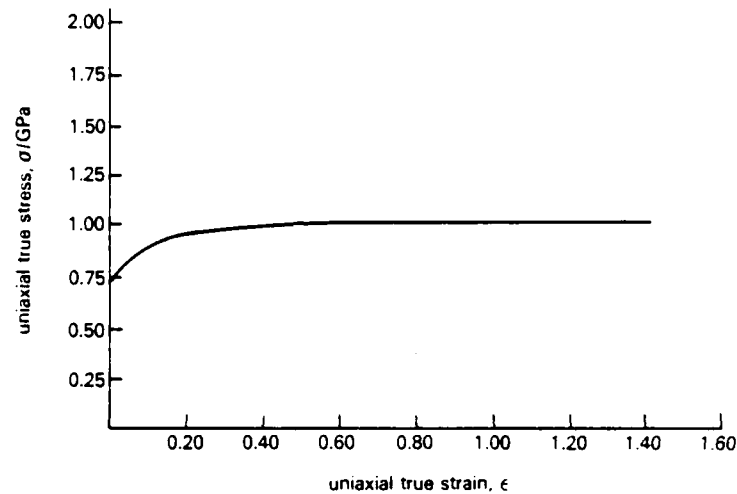


Fig. 10 — Solution curve for uniaxial continuum true stress-true strain response of HY-100 steel

The photographs taken of the tensile specimens strongly suggest the concept of a fully developed neck. Geometric similitude is in evidence for all but the specimens with a gage length of 1.27 cm (0.50in) and a diameter of 1.78 cm (0.70in). This specimen geometry had the lowest L_0/D_0 ratio, and featured the lowest percent reduction of area on the average. Further examination of this geometric similitude in the neck profile tends to support a view that the length of the neck remains a constant multiple of the original specimen diameter. The inflection points of the deformed specimen contour, which appear above and below the minimum specimen diameter at the neck, remain separated by a constant distance Δ from incipient necking to specimen fracture (Fig. 11).

Table 1 — Solution curve, in tabular form, for uniaxial true stress-true plastic strain response for HY-100 steel

Uniaxial True Stress, σ		Uniaxial True Plastic Strain, ϵ
$7.171 \times 10^8 \text{ N/m}^2$	$(1.040 \times 10^5 \text{ lb/in}^2)$	0.0000
7.929	$(1.150 \times 10^5 \text{ lb/in}^2)$	0.0240
8.343	$(1.210 \times 10^5 \text{ lb/in}^2)$	0.0500
8.964	$(1.300 \times 10^5 \text{ lb/in}^2)$	0.0955
9.101	$(1.350 \times 10^5 \text{ lb/in}^2)$	0.1410
9.550	$(1.385 \times 10^5 \text{ lb/in}^2)$	0.1738
9.605	$(1.393 \times 10^5 \text{ lb/in}^2)$	0.2060
9.687	$(1.405 \times 10^5 \text{ lb/in}^2)$	0.2386
9.825	$(1.425 \times 10^5 \text{ lb/in}^2)$	0.3034
9.963	$(1.445 \times 10^5 \text{ lb/in}^2)$	0.3682
1.002×10^9	$(1.454 \times 10^5 \text{ lb/in}^2)$	0.4332
1.007	$(1.460 \times 10^5 \text{ lb/in}^2)$	0.4981
1.011	$(1.467 \times 10^5 \text{ lb/in}^2)$	0.5631
1.016	$(1.473 \times 10^5 \text{ lb/in}^2)$	0.6280
1.017	$(1.475 \times 10^5 \text{ lb/in}^2)$	0.8300
1.018	$(1.477 \times 10^5 \text{ lb/in}^2)$	1.1420
1.020	$(1.479 \times 10^5 \text{ lb/in}^2)$	1.6620
1.021	$(1.481 \times 10^5 \text{ lb/in}^2)$	2.7020

Elastic modulus, $E = 1.80 \times 10^{11} \text{ N/m}^2$ ($26.1 \times 10^6 \text{ lb/in}^2$)

Poisson ratio, $\nu = 0.3$

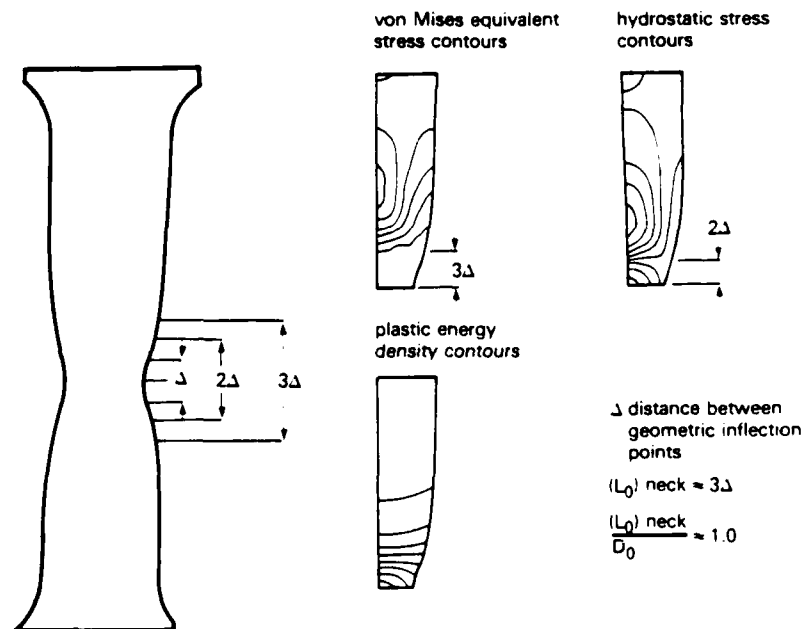


Fig. 11 — Definition of tensile specimen neck length based on geometric features and deformation

The inflection points, while providing the intrinsic geometric reference length for the neck, do not fully distinguish the actively flowing material of the neck from the material outside from the neck. Outside the neck, flow has ceased and unloading is in progress as the axial stress acting on the specimen cross section decreases with the global load due to neck development. In fact, for the HY-100 specimens of L_0/D_0 ratio greater than one, additional reference lengths based on the stress (or strain) states in the neck provide a more complete picture on which to define a neck length. Specifically, the hydrostatic stress contours which are bounded and contain the center of the neck extend over a total length 2Δ centered on the minimum diameter plane. The von Mises equivalent stress, which under the assumptions of plasticity theory as employed in the computational simulations govern the plastic deformation, is essentially uniform over a distance 3Δ , centered on the plane of minimum diameter. The neck radius at both ends of this distance is almost that of the specimen outside the neck.

From a phenomenological point of view, this last observation provides a functional definition of the neck based on an intrinsic length over which energy is actively dissipated. For the particular material under consideration this length is 3Δ , or three times greater than the intrinsic geometric length parameter Δ defined from the inflection point separation on the specimen profile. Thus, prior to the onset of necking the energy dissipation throughout the specimen is driven by axial extension. As the neck develops energy dissipation is confined to the neck, promoted by lateral contraction of the neck.

Working backward from the final specimen profile, the initial length of the neck $(L_0)_{\text{neck}}$ on the undeformed specimen can be calculated, and the ratio $(L_0)_{\text{neck}}/D_0$ determined. For the HY-100 material under consideration,

$$\frac{(L_0)_{\text{neck}}}{D_0} \approx 1.0. \quad (17)$$

This implies that for a fully developed neck to form,

$$\frac{L_0}{D_0} \geq \frac{(L_0)_{\text{neck}}}{D_0} \quad (18)$$

That is to say, the specimen aspect ratio must be at least that required for a fully developed neck. The specimen L_0/D_0 ratio fell below 1.0 only for the $L_0 = 1.27$ cm (0.50in), $D_0 = 1.78$ cm (0.70in) specimens from the full set of over three dozen specimens featuring twelve different

CONTINUUM MATERIAL TOUGHNESS CONCEPTS

The strain energy per unit mass at a given instant during deformation, will be

$$w = \lim_{\Delta V \rightarrow 0} \left[\frac{1}{\rho} \frac{\Delta W}{\Delta V} \right] \quad (19)$$

$$w = \int_0^{\epsilon_{ij}} \frac{\sigma_{ij}}{\rho} d\epsilon_{ij} \quad (20)$$

where ρ is the mass density, W is energy and V is volume. This energy density incorporates both stress and strain into a fundamental quantity relevant to thermodynamic descriptions of material deformation and damage. The energy density is a scalar quantity which takes into account all components of the stress and strain tensors in a physically consistent manner.

Failure of the material due to fracture, at the continuum scale, can be associated with the value of the energy density at which fracture occurs. Thus, the material toughness is defined as

$$w_c = \int_0^{(\epsilon_{ij})_c} \frac{\sigma_{ij}}{\rho} d\epsilon_{ij} \quad (21)$$

where w_c is the critical strain energy density value.

For ductile metals, the material density varies only slightly, even over large deformations. For this reason, it is common to define an energy per unit volume density

$$w = \lim_{\Delta V \rightarrow 0} \left[\frac{\Delta W}{\Delta V} \right] \quad (22)$$

$$= \int_0^{\epsilon_{ij}} \sigma_{ij} d\epsilon_{ij}, \quad (23)$$

with an associated critical value

$$w_c = \int_0^{(\epsilon_{ij})_c} \sigma_{ij} d\epsilon_{ij}. \quad (24)$$

The energy per unit mass is fundamental, but the energy per unit volume is equally appropriate for constant volume deformation processes.

The use of an energy density criterion for continuum fracture is consistent with the ideas expressed by Freudenthal (1950) on material behavior and scaling considerations. Gillemot (1976) examined cylindrical tensile specimens using analytical and empirical techniques. The strain energy density per unit volume, absorbed by the material up to the instant of fracture, was calculated from global specimen response and deformation geometry. Calculations of critical strain energy density values from computational simulations, however, are able to address the large deformation continuum toughness in detail appropriate for structural integrity analysis. Applications to structural integrity prediction, using continuum material toughness concepts as outlined here, include investigations by Matic and Jolles (1987a, 1987b) into the defect tolerance of welded components and the role of material, geometry and applied load on weld system performance.

For a multiaxial state of stress, each of the six stress-strain pairs, three normal and three shear, must be evaluated and summed, i.e.

$$\begin{aligned} w_c = & \int_0^{(\epsilon_{11})_c} \sigma_{11} d\epsilon_{11} + \int_0^{(\epsilon_{22})_c} \sigma_{22} d\epsilon_{22} + \int_0^{(\epsilon_{33})_c} \sigma_{33} d\epsilon_{33} + \\ & + \int_0^{(\epsilon_{12})_c} \sigma_{12} d\epsilon_{12} + \int_0^{(\epsilon_{23})_c} \sigma_{23} d\epsilon_{23} + \int_0^{(\epsilon_{31})_c} \sigma_{31} d\epsilon_{31}. \end{aligned} \quad (25)$$

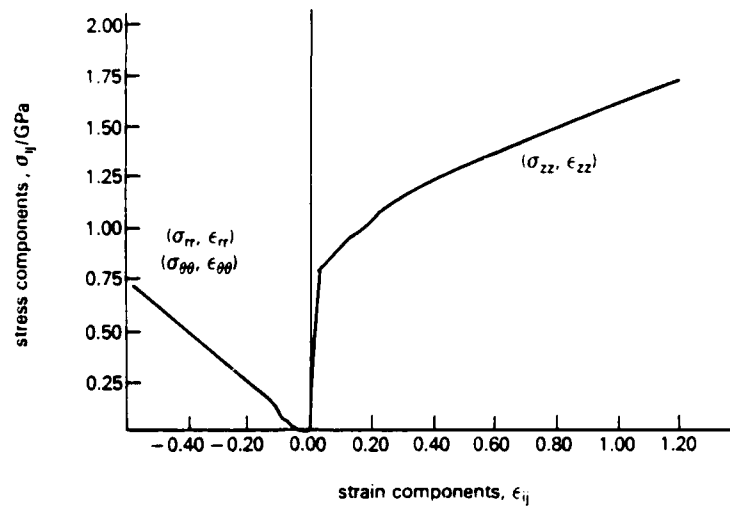
It should be noted that one or more individual terms in the multiaxial expression can be negative.

Their total, w_c , must be positive, however.

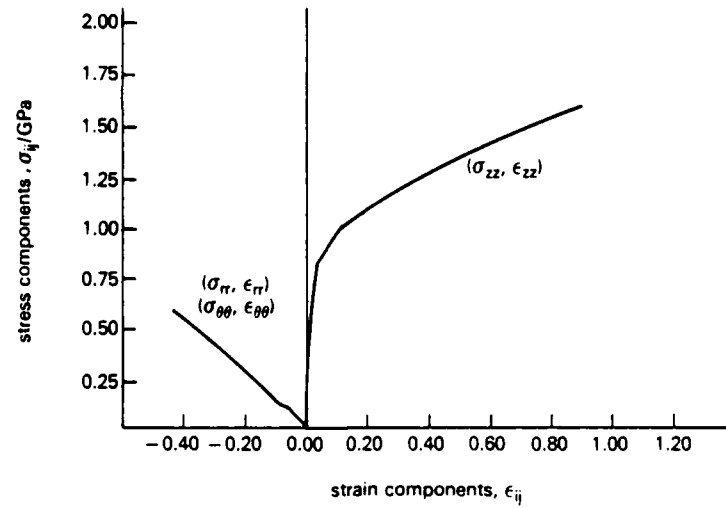
Tensile specimen failure is known to initiate at the center of the specimen neck, where the stresses and strains are multiaxial in character. The stresses and strains are plotted for the two 1.78 cm (0.70in) diameter specimens for finite element integration point nearest to the center of the specimen (Fig. 12). Symmetry conditions at the center of these specimens are reflected in the absence of any significant shear stress or strain components. The L_0/D_0 ratios for these specimens are 0.72 and 2.86, respectively. The lower ratio specimen is below the threshold ratio of 1.0 for fully developed necking. The higher ratio specimen is above the threshold.

All strain magnitudes are monotonically increasing over the deformation history. For the low L_0/D_0 specimen, the absence of a fully developed neck results in monotonically increasing values of stress over the entire deformation. Integration of these curves yields a critical energy density at the fracture initiation site of $8.89 \times 10^8 \text{ N-m/m}^3$ ($1.29 \times 10^5 \text{ lb-in/n}^3$). For the high L_0/D_0 specimen, the presence of a fully developed neck is preceded by essentially uniaxial deformation. As a result, the z component of stress monotonically increases while the r and θ components of stress are initially zero and monotonically increase only after necking has begun. Integration yields a critical energy density of $1.20 \times 10^9 \text{ N-m/m}^3$ ($1.74 \times 10^4 \text{ lb-in/n}^3$).

Essentially proportional loading is present in the low L_0/D_0 specimen stress state. Distinctly nonproportional loading is evident for the high L_0/D_0 specimen. The difference in the critical energy density is significant, particularly in light of the relative insensitivity of the stress-strain components to different loading histories. The difference in the two sets of stress-strain plots occurs for the r and θ components and is probably an indication of different energy dissipation mechanisms being developed during the initial deformation and yielding of each specimen. While on the larger scale the difference between the plots may appear small, in an energy sense it is much greater. The sensitivity of the continuum material toughness to nonproportional deformation histories has significant implications for fracture initiation, crack growth and structural integrity predictions.



(a)



(b)

Fig. 12 — Triaxial stress-strain histories at the center of the neck (a) for nonproportional triaxiality in the case of $L_0/D_0 = 2.86$ and (b) proportional triaxiality in the case of $L_0/D_0 = 0.71$

SUMMARY

A hybrid computational-experimental approach for the determination of material uniaxial constitutive parameters is applied to the interpretation of tensile test specimens of different sizes and geometries. The iterative development of a single unique material true stress-true strain curve for which computational predictions agree with experiment data for different specimens was discussed. The unique solution curve for HY-100 steel is presented.

The tensile specimen neck is observed to be geometrically invariant to size and geometry effects if the specimen L_0/D_0 aspect ratio is greater than one. This ratio defines a lower bound for a fully developed neck. An upper bound for the L_0/D_0 ratio exists in terms of specimen deformation symmetry. Evidence for this upper bound was observed computationally and confirmed from experiment data.

Continuum material toughness concepts were discussed in terms of the critical energy density to produce fracture. Computational reconstruction of the stress-strain histories leading to fracture initiation for the HY-100 specimens strongly suggest that the critical energy density is different for an arbitrary nonproportional deformation history when compared to a proportional deformation history. This seems to be true despite the general insensitivity of the stress-strain components to the different loading histories encountered.

REFERENCES

- [1] Bridgman P.W., 1952; *Studies in Large Plastic Flow and Fracture*, New York: McGraw Hill.
- [2] Filon L.N.G., 1902; On the Elastic Equilibrium of Circular Cylinders Under Certain Practical Systems of Load, *Phil. Trans.*, A198, 147-233.

- [3] Freudenthal A.M., 1950; *The Inelastic Behavior of Engineering Materials and Structures*, New York: Wiley.
- [4] Gillemot L.F., 1976; Criterion of Crack Initiation and Spreading, *Engng. Fracture Mech.*, **8**, 239-253.
- [5] Hibbitt H.D., Karlsson B.I., and Sorenson E.P., 1984a; *ABAQUS Theory Manual*, Providence: Hibbitt, Karlsson and Sorenson, Inc.
- [6] Hibbitt H.D., Karlsson B.I., and Sorenson E.P., 1984b; *ABAQUS User's Manual*, Providence: Hibbitt, Karlsson and Sorenson, Inc.
- [7] Hutchinson J.W., 1979; Survey of Some Recent Work on the Mechanics of Necking, *Proc. 8th U.S. Natl. Congr. of Appl. Mech.*, pp 87-98 Noth Hollywood: West Period.
- [8] Hutchinson J.W., and Neale K.W., 1983; Neck Propagation, *J. Mech. Phys. Solids*, **31**, 405-426.
- [9] Kleiber M., 1986; On Plastic Localization and Failure in Plane Strain and Round Void Containing Tensile Bars, *Int. J. Plasticity*, **2**, 205-221, NRL Memo. Rpt. 5937.
- [10] Matic P., 1985; Numerically Predicting Ductile Material Behavior from Tensile Specimen Response, *J. Th. Appl. Fracture Mech.*, **4**, 13-28.
- [11] Matic P., and Jolles M.I., 1986; The Influence of Small Defects on Tensile Specimen Ductility and Symmetry of Deformation, *NRL Memo. Rpt. 5937*.
- [12] Matic P. and Jolles M.I., 1987a; Defect Constitutive Behavior and Continuum Toughness Considerations for Weld Integrity Analysis, *Proc. 3rd Int. Symp. on Nonlinear Fracture*, Philadelphia: American Society for Testing and Materials. (In press)

- [13] Matic P. and Jolles M.I., 1987b; The Influence of Weld Metal Properties, Weld Geometry and Applied Load on Weld System Performance, *NRL Memo. Rpt. No. 5987*.
- [14] Needleman A., 1972; A Numerical Study of Necking in Circular Cylindrical Bars, *J. Mech. Phys. Solids*, **20**, 111-127.
- [15] Needleman A., and Becker R., 1986; Effect of Yield Surface Curvature on Necking and Failure in Porous Plastic Solids, *J. Appl. Mech*, **53**, 491-498.
- [16] Norris D.M., Moran B., Scudder J.K. and Quinones D.F., 1978; A Computer Simulation of the Tension Test, *J. Mech. Phys. Solids*, **26**, 1-19.
- [17] Tvergaard V., and Needleman, A., 1984; Analysis of the Cup-Cone Fracture in a Round Tensile Bar, *Acta Metall*, **32**, 157-169.

APPENDIX I

ABAQUS Finite Element Program Formulation

A brief summary of the ABAQUS finite element program is included here for reference and completeness in view of the various possible theoretical formulations available for geometrically and materially nonlinear analysis. The reader is referred to Hibbitt et al (1984a) for further details.

For a material particle at reference position X_i at time t equal to zero, its current position x_i at a later time may be expressed as

$$x_i = x_i(X_i, t). \quad (A1)$$

An orthogonal coordinate system of unit base vectors is assumed. The relative position dx_i between two material particles in their current configuration may be expressed in terms of their relative position in their reference configuration

$$dx_i = \frac{\partial x_i}{\partial X_j} dX_j \quad (A2)$$

$$= F_{ij} dX_j \quad (A3)$$

where F_{ij} is defined as the deformation gradient.

The velocity of the material particle will be

$$v_i = \frac{\partial x_i}{\partial t} \quad (A4)$$

The incremental velocity between two particles will be

$$dv_i = \frac{\partial v_i}{\partial X_j} dX_j \quad (\text{A5})$$

$$= \frac{\partial v_i}{\partial x_j} \frac{\partial x_j}{\partial X_k} dX_k \quad (\text{A6})$$

$$= L_{ij} F_{jk} dX_k \quad (\text{A7})$$

where L_{ij} is the velocity gradient at a material point in the body. The velocity gradient may be decomposed into the sum of its symmetric and antisymmetric tensor components as

$$L_{ij} = \frac{1}{2} (L_{ij} + L_{ji}) + \frac{1}{2} (L_{ij} - L_{ji}) \quad (\text{A8})$$

$$= \frac{1}{2} (v_{i,j} + v_{j,i}) + \frac{1}{2} (v_{i,j} - v_{j,i}) \quad (\text{A9})$$

$$= D_{ij} + \Omega_{ij} \quad (\text{A10})$$

where D_{ij} is the rate of deformation tensor, associated with material straining, and Ω_{ij} is the material spin tensor associated with pure rotation at the material point.

For a material body of volume V and surface S in its current configuration, force equilibrium in integral form is given by

$$\int_S t_i dS + \int_V f_i dV = 0 \quad (\text{A11})$$

where t_i is the surface traction vector per unit of current area and f_i is the body force vector per unit of current volume. The Cauchy stress tensor σ_{ij} is related to t_i by

$$t_i = \sigma_{ij} n_j \quad (\text{A12})$$

where n_j is the outward unit vector normal to surface S . Using (A12) in (A11) along with Gauss' theorem to transform the surface integral to a volume integral,

$$\int_V (\sigma_{ij,j} + f_i) dV = 0. \quad (A13)$$

The integral must, in general, be zero. Therefore,

$$\sigma_{ij,j} + f_i = 0. \quad (A14)$$

Moment equilibrium in integral form requires

$$\int_S x_i t_j e_{ijk} dS + \int_V x_i f_j e_{ijk} dV = 0 \quad (A15)$$

where e_{ijk} is the permutation symbol. Using Gauss' theorem

$$\int_V (x_i, l \sigma_{jl} e_{ijk} + x_i \sigma_{jl, l} e_{ijk} + x_i \sigma_{jl} e_{ijk, l} + x_i f_j e_{ijk}) dV = 0 \quad (A16)$$

Evaluating each term in this expression and using (A14) provides that σ_{ij} must be symmetric, i.e.

$$\sigma_{ij} = \sigma_{ji} \quad (A17)$$

The differential force equilibrium expression (A14) is used to generate a virtual work expression by taking the dot product with a virtual velocity, v_i^* , and integrating over the volume. This takes the form, after application of Gauss' theorem,

$$\int_V \left[(\sigma_{ij} v_i^*),_{,j} - \sigma_{ij} v_{i,j}^* + f_i v_i^* \right] dV = 0. \quad (A18)$$

The virtual velocity field must satisfy continuity and prescribed velocity requirements. Expressing the first integral in terms of tractions and rearranging

$$\int_V \sigma_{ij} v_{i,j}^* dV = \int_S t_i v_i^* dS + \int_V f_i v_i^* dV \quad (A19)$$

From the definition of the velocity gradient, the virtual velocity gradient is

$$\dot{v}_{i,j} = L_{ij} \quad (A20)$$

$$= D_{ij}^* + \Omega_{ij}^* \quad (A21)$$

where the virtual rate of deformation, D_{ij}^* , is symmetric and the virtual spin, Ω_{ij}^* , is antisymmetric. In light of the Cauchy stress tensor symmetry, it follows that

$$\int_V \sigma_{ij} D_{ij}^* dV = \int_S t_i \dot{v}_i dS + \int_V f_i \dot{v}_i dV. \quad (A22)$$

The left hand side of this expression is converted to an integral taken over the reference volume V_o , i.e.

$$\int_{suV} V_o \sigma_{ij} D_{ij}^* J dV_o = \int_S t_i \dot{v}_i dS + \int_V f_i \dot{v}_i dV. \quad (A23)$$

where J is the determinant of the Jacobian. J is equal to the ratio of the differential volumes in the reference and current configuration.

The Kirchhoff (or Trefftz) stress is defined as

$$\tau_{ij} = J \sigma_{ij}. \quad (A24)$$

Therefore,

$$\int_{V_o} \tau_{ij} D_{ij}^* dV_o = \int_S t_i \dot{v}_i dS + \int_V f_i \dot{v}_i dV \quad (A25)$$

The Kirchhoff stress, τ_{ij} , is equal to the Cauchy stress, σ_{ij} , when J is equal to unity. For the material behavior considered in this analysis J deviates from unity by only a small amount. Therefore, the constitutive formulation in terms of Cauchy stress, as described in the main body of this paper will be applicable when expressed in terms of Kirchhoff stress.

Equation (A26) is the virtual velocity equilibrium equation and is the basis for interpolation and discretization for the finite element formulation. The virtual velocity at a point inside an element will be interpolated as

$$v_i^* = N_{ij} \bar{v}_j^* \quad (\text{A26})$$

where the summation is understood to involve only those nodal values \bar{v}_j^* relevant to a particular element. The virtual rate of deformation becomes

$$D_{ij}^* = \frac{1}{2} (N_{ik} \bar{v}_k^*)_{,j} + (N_{jk} \bar{v}_k^*)_{,i} \quad (\text{A27})$$

$$= \frac{1}{2} (N_{ik,j} + N_{jk,i}) \bar{v}_k^* \quad (\text{A28})$$

Therefore, (A25) becomes

$$\int_{V_0} \frac{1}{2} \tau_{ij} (N_{ik,j} + N_{jk,i}) \bar{v}_k^* dV_0 = \int_S t_i N_{ik} \bar{v}_k^* dS + \int_V f_i N_{ik} \bar{v}_k^* dV \quad (\text{A29})$$

or, since \bar{v}_k^* appears in each integral,

$$\int_{V_0} \frac{1}{2} \tau_{ij} (N_{ik,j} + N_{jk,i}) dV_0 = \int_S t_i N_{ik} dS + \int_V f_i N_{ik} dV. \quad (\text{A30})$$

The integrations are taken with respect to the discretized volumes and surfaces consistent with element and nodal definitions.

Equation (A30) forms the basis for the finite element solution. An incremental solution is generated by the Newton algorithm. The Jacobian of (A30) is required for the incremental solution, and results in the introduction of a Kirchhoff stress rate, $\dot{\tau}_{ij}$, into the incremental equilibrium equation.

The stress rate takes the form

$$\dot{\tau}_{ij} = \overset{\nabla}{\tau}_{ij} + \Omega_{ik} \tau_{kj} + \tau_{ik} \Omega_{jk} \quad (\text{A31})$$

where $\dot{\tau}_{ij}$ is the total stress rate, $\overset{\nabla}{\tau}_{ij}$ is the material (or Jaumann) stress rate associated with the material response through the constitutive formulation. The remaining terms involving Ω_{ij} are stress rate contributions due to rotation. In practice, all constitutive calculations are performed using $\overset{\nabla}{\tau}_{ij}$.

The total strain measure ϵ_{ij} is calculated in a manner consistent with the integration of D_{ij} . This generates logarithmic strain measures which are energy conjugate to the Kirchoff stress τ_{ij} which, as discussed above, is approximately equal to the Cauchy stress σ_{ij} in the analyses under consideration.

APPENDIX II

Laboratory Specimen Imperfections

Prior to testing, the tensile test specimen gage section diameters were measured. Deviations from the nominal specimen gage diameter D_0 are tabulated below for each specimen as the maximum and minimum specimen diameters, $(D_0)_{\max}$ and $(D_0)_{\min}$, measured along the gage length. The diameter imperfection d_0 is defined as

$$d_0 = \frac{(D_0)_{\max} - (D_0)_{\min}}{(D_0)_{\max} + (D_0)_{\min}} \quad (\text{AII.1})$$

This may be interpreted as the average deviation (from the average diameter) divided by the average diameter.

The specimens modeled for the computational simulations were assumed to be free of any geometric imperfections. The scatter of neck eccentricity values with respect to the computational predictions of neck eccentricity values, as discussed above, are consistent with the small imperfections in the specimen diameters listed in Table AII-1.

Table AII-1. Maximum measured diameter imperfection value of laboratory specimens.
Specimens not measured prior to testing are denoted by "--" values.

Nominal Gage Length, L_0	Nominal Gage Diameter, D_0	Maximum Gage Diameter, $(D_g)_{\max}$	Minimum Gage Diameter, $(D_g)_{\min}$	Diameter Imperfection, d_0
1.27 cm (0.50 in)	0.76 cm (0.30 in)	0.770 cm (0.303 in)	0.765 cm (0.301 in)	0.003
		0.767 cm (0.302 in)	0.762 cm (0.300 in)	0.003
		0.772 cm (0.304 in)	0.767 cm (0.302 in)	0.003
	1.27 cm (0.50 in)	1.275 cm (0.502 in)	1.270 cm (0.500 in)	0.002
		1.285 cm (0.506 in)	1.280 cm (0.504 in)	0.002
		1.275 cm (0.502 in)	1.275 cm (0.502 in)	0.000
	1.78 cm (0.70 in)	1.778 cm (0.700 in)	1.778 cm (0.700 in)	0.000
		1.791 cm (0.705 in)	1.786 cm (0.703 in)	0.001
		1.786 cm (0.703 in)	1.781 cm (0.701 in)	0.001
		1.773 cm (0.698 in)	1.770 cm (0.697 in)	0.001
		1.783 cm (0.702 in)	1.783 cm (0.702 in)	0.000
		1.783 cm (0.702 in)	1.783 cm (0.702 in)	0.000
2.54 cm (1.00 in)	0.76 cm (0.30 in)	0.767 cm (0.302 in)	0.762 cm (0.300 in)	0.003
		0.777 cm (0.306 in)	0.767 cm (0.302 in)	0.006
		0.767 cm (0.302 in)	0.762 cm (0.300 in)	0.003
	1.27 cm (0.50 in)	1.278 cm (0.503 in)	1.267 cm (0.499 in)	0.004
		1.270 cm (0.500 in)	1.267 cm (0.499 in)	0.001
		1.295 cm (0.510 in)	1.265 cm (0.498 in)	0.012
	1.78 cm (0.70 in)	1.786 cm (0.703 in)	1.778 cm (0.700 in)	0.002
		1.783 cm (0.702 in)	1.775 cm (0.699 in)	0.002
		1.773 cm (0.698 in)	1.770 cm (0.697 in)	0.001
3.81 cm (1.50 in)	0.76 cm (0.30 in)	0.775 cm (0.305 in)	0.765 cm (0.301 in)	0.007
		0.775 cm (0.305 in)	0.765 cm (0.301 in)	0.007
		0.772 cm (0.304 in)	0.767 cm (0.302 in)	0.003
	1.27 cm (0.50 in)	1.280 cm (0.504 in)	1.275 cm (0.502 in)	0.002
		1.283 cm (0.505 in)	1.273 cm (0.501 in)	0.004
		1.270 cm (0.500 in)	1.260 cm (0.496 in)	0.004
	1.78 cm (0.70 in)	1.786 cm (0.703 in)	1.786 cm (0.700 in)	0.002
		1.778 cm (0.700 in)	1.773 cm (0.698 in)	0.001
		1.793 cm (0.706 in)	1.781 cm (0.701 in)	0.004
5.08 cm (2.00 in)	0.76 cm (0.30 in)	0.777 cm (0.306 in)	0.762 cm (0.300 in)	0.010
		0.765 cm (0.301 in)	0.757 cm (0.298 in)	0.005
		—	—	—
	1.27 cm (0.50 in)	1.273 cm (0.501 in)	1.260 cm (0.496 in)	0.005
		1.275 cm (0.502 in)	1.265 cm (0.498 in)	0.004
		1.283 cm (0.505 in)	1.273 cm (0.501 in)	0.004
	1.78 cm (0.70 in)	1.796 cm (0.707 in)	1.765 cm (0.695 in)	0.009
		1.791 cm (0.705 in)	1.778 cm (0.700 in)	0.004
		1.770 cm (0.697 in)	1.763 cm (0.694 in)	0.002

END

DATE
FILMED

DEC.

1987